

## CHEMISTRY

## Self-assembly of electronically abrupt borophene/organic lateral heterostructures

Xiaolong Liu,<sup>1</sup> Zonghui Wei,<sup>1</sup> Itamar Balla,<sup>2</sup> Andrew J. Mannix,<sup>2,3</sup> Nathan P. Guisinger,<sup>3</sup> Erik Luijten,<sup>1,2,4,5</sup> Mark C. Hersam<sup>1,2,6,7\*</sup>

2017 © The Authors, some rights reserved; exclusive licensee American Association for the Advancement of Science. Distributed under a Creative Commons Attribution NonCommercial License 4.0 (CC BY-NC).

Two-dimensional boron sheets (that is, borophene) have recently been realized experimentally and found to have promising electronic properties. Because electronic devices and systems require the integration of multiple materials with well-defined interfaces, it is of high interest to identify chemical methods for forming atomically abrupt heterostructures between borophene and electronically distinct materials. Toward this end, we demonstrate the self-assembly of lateral heterostructures between borophene and perylene-3,4,9,10-tetracarboxylic dianhydride (PTCDA). These lateral heterostructures spontaneously form upon deposition of PTCDA onto submonolayer borophene on Ag(111) substrates as a result of the higher adsorption enthalpy of PTCDA on Ag(111) and lateral hydrogen bonding among PTCDA molecules, as demonstrated by molecular dynamics simulations. In situ x-ray photoelectron spectroscopy confirms the weak chemical interaction between borophene and PTCDA, while molecular-resolution ultrahigh-vacuum scanning tunneling microscopy and spectroscopy reveal an electronically abrupt interface at the borophene/PTCDA lateral heterostructure interface. As the first demonstration of a borophene-based heterostructure, this work will inform emerging efforts to integrate borophene into nanoelectronic applications.

## INTRODUCTION

The rapid ascent of graphene has driven extensive interest in additional atomically thin elemental two-dimensional (2D) materials, including phosphorene (1), stanene (2), and, most recently, borophene (3, 4). Unlike the naturally layered structures of bulk graphite and black phosphorus, boron exhibits significantly more complex and diverse bulk structures due to the rich bonding configurations among boron atoms (5–7). Studies of atomically thin boron sheets (that is, borophene) relied primarily on theoretical predictions (8–10) until recent studies experimentally demonstrated borophene synthesis on Ag(111) substrates. These experimental studies (3, 4) have confirmed theoretical predictions that borophene is a 2D metal and can adopt multiple structurally distinct phases as a function of processing conditions (8, 10).

As an emerging 2D material, borophene has thus far been studied only in isolation; nearly all technological applications, however, will require the integration of borophene with other materials. Of particular interest are electronically abrupt lateral heterostructures, which have been widely explored in other 2D materials because of their novel electronic properties (11–15). For example, atomically well-defined lateral heterostructures between graphene and hexagonal boron nitride (11) have revealed spatially confined boundary states with scanning tunneling spectroscopy (STS) (16). However, it should be noted that methods to experimentally realize atomically clean and abrupt lateral heterojunctions remain challenging for many 2D material systems (12, 14, 15, 17). For example, the growth front of the first 2D material can be easily contaminated, which can disrupt the subsequent growth of the second 2D material and/or lead to ill-defined interfacial regions.

Alloying and intermixing during the growth of 2D material lateral heterostructures also prevent abrupt interfaces (13, 18).

We report here the first experimental demonstration and characterization of a borophene lateral heterostructure with the molecular semiconductor perylene-3,4,9,10-tetracarboxylic dianhydride (PTCDA). Initially, submonolayer homogeneous-phase borophene is grown on Ag(111) on mica substrates by electron beam evaporation of a pure boron source, resulting in atomically pristine 2D boron sheets, as confirmed by in situ x-ray photoelectron spectroscopy (XPS). Subsequent deposition of PTCDA results in preferential assembly on Ag(111), ultimately resulting in the presence of dense and well-ordered PTCDA monolayers that form lateral heterostructures with the borophene flakes. PTCDA is known to self-assemble on a variety of substrates, including metals (19), semimetals (20), semiconductors (21), oxides (22), and salt crystals (23). The fact that it does not self-assemble on borophene is thus initially unexpected but leads to the desirable formation of lateral heterostructures with borophene.

It has been reported that the electronic properties of self-assembled monolayers can be tuned by neighboring materials (24). In particular, the noncovalent interaction of PTCDA with silver substrates leads to a delocalized 2D band state with a parabolic dispersion (25). It should also be noted that noncovalent van der Waals interactions are prevalent in electronic devices based on 2D (26, 27) and mixed-dimensional heterostructures (28). For example, van der Waals-coupled organic lateral heterostructures have been demonstrated as gate-tunable p-n diodes (17). It has also been reported that van der Waals-coupled electronic states play an important role in determining the electronic structure and optical properties of double-walled carbon nanotubes (29). For the case of borophene and PTCDA, in situ XPS verifies the absence of covalent bonding between borophene and PTCDA because the B 1s peak remains virtually unchanged following the formation of borophene/PTCDA lateral heterostructures. Using molecular dynamics (MD) simulations, we demonstrate that these observations are consistent with a lower adsorption enthalpy of PTCDA on borophene and the formation of a hydrogen bonding network between adsorbed PTCDA molecules. Ultrahigh-vacuum (UHV) scanning tunneling microscopy (STM) and STS measurements further show

<sup>1</sup>Applied Physics Graduate Program, Northwestern University, Evanston, IL 60208, USA. <sup>2</sup>Department of Materials Science and Engineering, Northwestern University, Evanston, IL 60208, USA. <sup>3</sup>Center for Nanoscale Materials, Argonne National Laboratory, Argonne, IL 60439, USA. <sup>4</sup>Department of Engineering Sciences and Applied Mathematics, Northwestern University, Evanston, IL 60208, USA. <sup>5</sup>Department of Physics and Astronomy, Northwestern University, Evanston, IL 60208, USA. <sup>6</sup>Department of Chemistry, Northwestern University, Evanston, IL 60208, USA. <sup>7</sup>Department of Electrical Engineering and Computer Science, Northwestern University, Evanston, IL 60208, USA.

\*Corresponding author. Email: m-hersam@northwestern.edu

that these lateral borophene/PTCDA heterostructures are electronically abrupt at the molecular scale. In addition to elucidating the unique chemistry of borophene, this work has clear implications for borophene-based nanoelectronics.

## RESULTS

### Homogeneous-phase borophene

The growth of borophene is shown schematically in Fig. 1A, where a boron flux created by electron beam evaporation of a pure boron rod is directed toward a Ag(111) thin film (~300 nm thick) on a mica substrate in UHV. The inset shows an atomic-resolution STM image of the atomically clean Ag(111) surface preceding boron deposition. By maintaining the substrate at a temperature of ~480°C, pure homogeneous-phase borophene [that is, the common phase realized in the initial experimental reports of borophene (3, 4)] is realized with surface coverage controlled by the deposition duration. The STM image in Fig. 1B shows a representative morphology of the resulting borophene growth both on and across atomically flat Ag(111) terraces. Atomic-scale STM imaging indicates a carpet-mode growth of homogeneous-phase borophene (fig. S1), which was previously observed for striped-phase borophene (3). Because of the convolution of electronic and physical structures in STM imaging, the borophene islands appear as depressions under these STM imaging conditions, a finding that is consistent with previous reports (3, 4). Furthermore, the borophene islands adopt elongated or truncated triangular shapes with aligned edges, which suggest registry between borophene and the underlying Ag(111) substrate.

The chemical integrity of the as-grown borophene is probed by in situ XPS, as shown in Fig. 1C. The B 1s core-level spectrum (top)

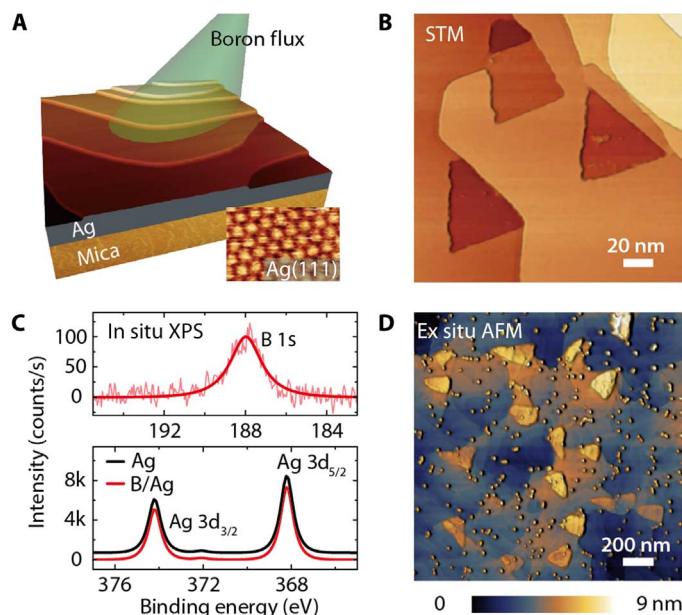


**Fig. 1. Homogeneous-phase borophene.** (A) Schematic of borophene growth on Ag(111) thin film on mica. Inset: Atomic-resolution STM image of the Ag(111) surface ( $V_s = 0.01$  V,  $I_t = 100$  pA). (B) STM image of triangular borophene islands on Ag(111). Under these imaging conditions ( $V_s = 1.2$  V,  $I_t = 160$  pA), the borophene islands appear as depressions. (C) In situ XPS spectra of the B 1s core level on pristine borophene (top) and Ag 3d core levels (vertically offset) before and after borophene growth (bottom). (D) Ex situ AFM image of borophene/Ag(111) with borophene islands appearing as protrusions.

shows a clear pristine boron peak (30) at ~188 eV with no peaks observed at higher binding energies of ~192 eV, which would otherwise correspond to oxidized boron (3, 4, 30, 31). The pristine nature of borophene is further confirmed by the absence of an oxygen peak in the O 1s core-level spectrum (fig. S2). The Ag 3d core-level spectra (Fig. 1C, bottom) before and after borophene growth reveal no detectable peak splitting, shifting, or broadening, which suggests the absence of B-Ag alloying and thus the formation of chemically distinct 2D boron layers (fig. S2). Figure 1D shows an ex situ atomic force microscopy (AFM) image of borophene after being exposed to air for ~20 min. Triangular protrusions indicate that the borophene islands are topographically protruding above the Ag surface. The particles observed in the AFM image likely result from boron particles during deposition (3, 4), ambient-induced contamination, or Ag oxidation.

Atomic-scale STM and STS characterization of borophene is provided in Fig. 2. The brick wall-like structure of homogeneous-phase borophene is shown in Fig. 2A, with the inset showing the fast Fourier transform. The measured interrow distances are 4.5 and 8.2 Å in the labeled **a** and **b** directions, respectively, consistent with previous reports (3, 4). Although this brick wall structure has been observed previously, additional atomic-scale contrast is observed under other bias conditions (fig. S3). A 60° grain boundary of borophene is shown in Fig. 2B, further suggesting that the sixfold symmetry of the Ag(111) substrate templates borophene growth. In addition to grain boundaries, another type of frequently observed 1D defect is provided in Fig. 2C. In the bottom image, the brick wall patterns and the line defects are highlighted with green ovals and green arrowheads, respectively. The line defects are parallel and running along the **b** direction. Aligned point defects (yellow arrowheads) are also found along these line defects (green arrowhead), as shown in Fig. 2D. The existence of these defects may provide strain relaxation that helps accommodate the lattice mismatch between borophene and Ag(111).

The electronic properties of homogeneous-phase borophene were further examined via STS. Figure 2E shows the current-voltage ( $I$ - $V$ ) measurements on both borophene and Ag(111), revealing the metallic behavior of borophene. The differential tunneling conductance curves of Ag(111) and borophene are provided in Fig. 2F. Borophene exhibits a nearly constant density of states (DOS) at small positive sample biases, while Ag(111) shows a feature that is consistent with literature reports of the known surface state starting below the Fermi level (32–34). These electronic differences are further demonstrated in Fig. 2G, where STS mapping over a borophene island at two different biases (–0.2 and 0.1 V) produces inverted contrast. STS maps over a continuous range of sample biases between –0.3 and 0.7 V are also shown in movie S1.

### Self-assembly of borophene/PTCDA lateral heterostructures

The deposition of PTCDA is achieved by thermally evaporating PTCDA molecules from an alumina-coated crucible. Fine-tuning of the evaporation temperature and duration allows precise, layer-by-layer growth of self-assembled PTCDA on Ag(111). Figure 3A shows a large-scale STM image following PTCDA deposition onto submonolayer borophene on a Ag(111) substrate. The large triangular domain at the lower half of the image is a bare borophene island surrounded by a PTCDA monolayer and a small patch of clean Ag(111). Atomic-resolution imaging of this borophene island (fig. S4) confirms the absence of PTCDA on the borophene surface.

The preferential assembly of PTCDA on Ag(111) compared to borophene leads to the spontaneous formation of borophene/PTCDA lateral heterostructures. Because of the presence of steps in the

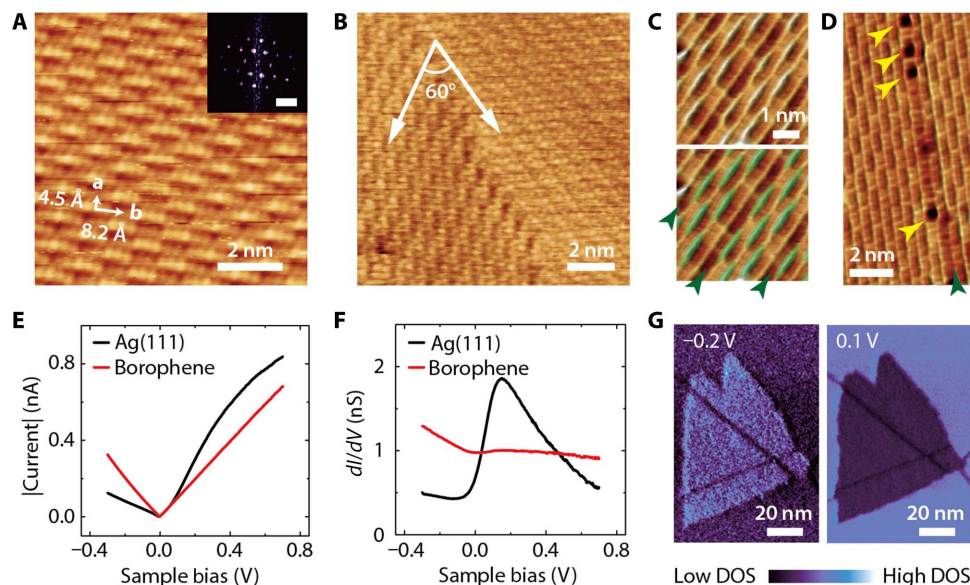


**Fig. 2. Structural and electronic properties of homogeneous-phase borophene.** (A) Atomic-resolution STM image of homogeneous-phase borophene showing the brick wall structure ( $V_s = -1.2$  V,  $I_t = 2.4$  nA). Inset: Fast Fourier transform of the image. Scale bar,  $2$  nm $^{-1}$ . (B) STM image showing a borophene  $60^\circ$  grain boundary ( $V_s = -0.15$  V,  $I_t = 3.0$  nA). (C) STM images showing line defects in borophene. Brick wall patterns and the line defects are highlighted with green ovals and arrowheads, respectively, in the bottom image ( $V_s = -1.1$  V,  $I_t = 500$  pA). (D) STM image showing aligned point defects along a line defect, as indicated by the yellow and green arrowheads, respectively ( $V_s = -60$  mV,  $I_t = 4.3$  nA). (E) Current-voltage and (F) differential tunneling conductance spectra of Ag(111) and borophene. (G) STS maps of borophene on Ag(111) at sample biases of  $-0.2$  and  $0.1$  V.

underlying Ag(111) substrate, the geometry of the borophene/PTCDA lateral heterostructure is better understood through the cross-sectional profile along the white dashed line (Fig. 3A), where each step height has been labeled. The measured step heights of  $2.4$  Å across the PTCDA layer (green arrowhead) and borophene region (blue arrowheads) correspond to a single atomic step height on Ag(111) ( $2.36$  Å) (35) as a result of the carpet-mode growth of PTCDA and borophene over Ag step edges (figs. S1 and S5). The apparent step height of  $2.3$  Å from borophene to the PTCDA monolayer (yellow arrowhead) is explained by the sum of the  $0.7$  Å step height from borophene to Ag(111) (fig. S6) and the  $1.6$  Å step height from Ag(111) to the PTCDA monolayer (gray arrowhead). Therefore, the borophene/PTCDA lateral heterostructure consists of borophene laterally interfacing with a monolayer of self-assembled PTCDA on Ag(111), as shown schematically in Fig. 3B. This situation is analogous to the preferential assembly of meso-tetramesitylporphyrins on clean Cu(001) compared to nitrogen-modified Cu(001), which has been attributed to the lower polarizability of nitrogen-modified Cu(001) and thus decreased van der Waals interaction with noncovalently bonded molecular adlayers (36).

The self-assembly motif adopted by PTCDA on Ag(111) is the well-known herringbone structure (25, 37). Figure 3C shows the unit cell of this structure, which is more directly observed in Fig. 3 (D and E). In particular, the green, yellow, and blue squares in Fig. 3D highlight regions of PTCDA, borophene, and bare Ag, respectively. The zoomed-in STM images of each region are shown in Fig. 3 (E to G), with the unit cell of PTCDA schematically overlaid in Fig. 3E. The relative lattice orientation of homogeneous-phase borophene and Ag(111) is denoted by the pairs of yellow and blue arrows in Fig. 3 (F and G), which are parallel to each other and thus indicate registry between the two materials. This apparent registry is consistent with

the aligned triangular domains in Fig. 1B and the formation of  $60^\circ$  grain boundaries in Fig. 2B, as noted above.

### MD modeling

To explore the effect of competing adsorption on the self-assembly of molecules on heterogeneous substrates, we used MD simulations at a fixed temperature of  $T = 300$  K, which matches the experimental conditions. Because we are interested in large-scale collective effects that are not accessible through ab initio calculations, we reduced the PTCDA molecules to a coarse-grained representation (fig. S7) capable of forming lateral hydrogen bonds as well as adsorption on the substrate. The Ag(111) substrate is represented as a hexagonally close-packed lattice, with an interatomic spacing of  $2.898$  Å. The excluded-volume interactions are modeled with shifted-truncated Lennard-Jones (LJ) potentials, and the attractions are represented by LJ potentials. Modeling details are described in Materials and Methods. While the hydrogen bonding strength is kept fixed, we systematically vary the enthalpy of adsorption per molecule,  $\Delta H_{\text{ads}}$ , which we define as the magnitude of the relative enthalpy  $\Delta H(z) = H(z) - H(\infty)$  upon adsorption at  $z = z_G$ . The relative Gibbs free energy  $\Delta G(z)$  and entropy  $\Delta S(z)$  are similarly defined. Here,  $z$  is the distance from the substrate, and  $z_G$  is the position where  $\Delta G(z)$  takes its minimum. To set the scale of  $\Delta H_{\text{ads}}$ , we first quantify the loss of entropy upon adsorption of a single coarse-grained PTCDA molecule via thermodynamic integration (see Materials and Methods). As shown in Fig. 4A, at  $\Delta H_{\text{ads}} = 10k_B T$ , we find a Gibbs free energy of adsorption  $\Delta G_{\text{ads}}$  of approximately  $4k_B T$ , implying an entropy loss of  $\sim 6k_B$  for a fully adsorbed PTCDA molecule. The functional form of the entropy loss (namely, logarithmic in surface separation  $z - z_G$ ) can be rationalized through estimation of the loss in degrees of freedom upon adsorption (fig. S8).

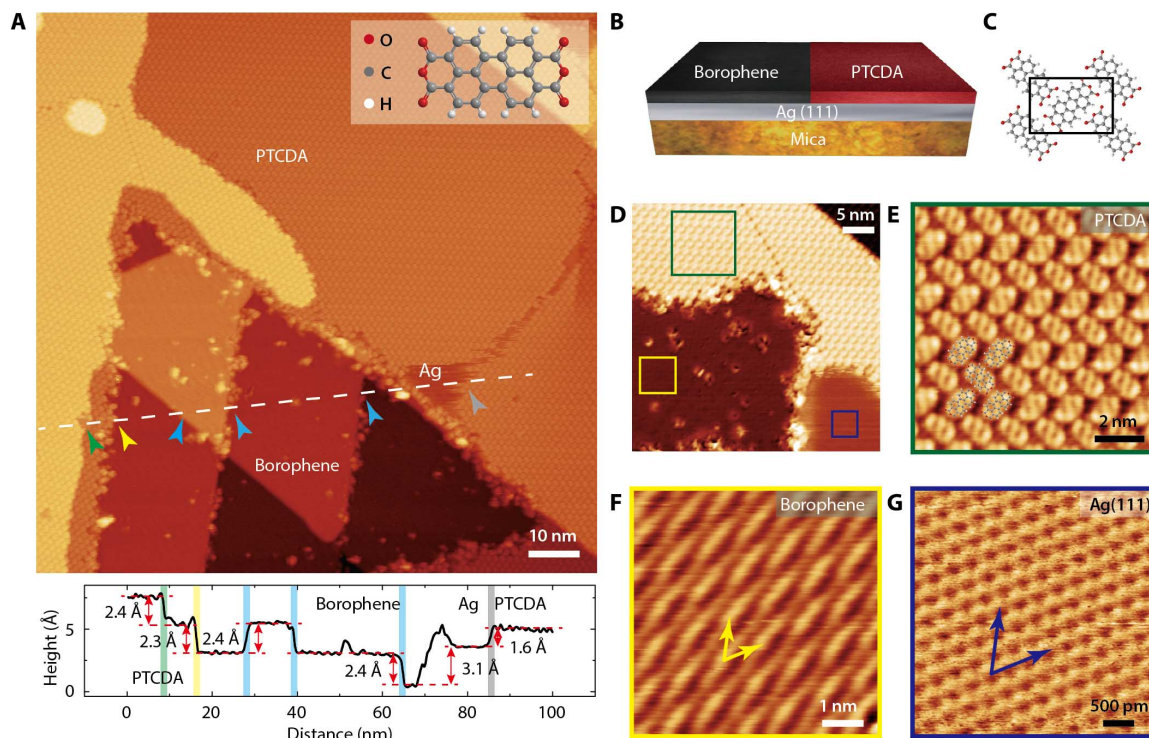


**Fig. 3. Borophene/PTCDA lateral heterostructure.** (A) Large-scale STM image of a borophene/PTCDA lateral heterostructure and the cross-sectional profile along the white dashed line ( $V_s = -1.7$  V,  $I_t = 90$  pA). Borophene-to-PTCDA step edges, Ag-to-PTCDA step edges, and Ag atomic step edges under PTCDA and borophene are indicated by the yellow, gray, green, and blue arrowheads, respectively. Inset: PTCDA molecule structure. (B) Schematic of a borophene/PTCDA lateral heterostructure. (C) Unit cell of the PTCDA herringbone structure. (D) STM image of a borophene/PTCDA lateral heterostructure with the green, yellow, and blue boxes indicating regions of PTCDA, borophene, and Ag, respectively ( $V_s = -1.1$  V,  $I_t = 90$  pA). (E to G) STM images of the square regions indicated in (D). The pairs of yellow and blue arrows indicate the lattice orientations of borophene and Ag(111) [(E)  $V_s = -0.45$  V,  $I_t = 140$  pA; (F)  $V_s = -1.1$  V,  $I_t = 500$  pA; (G)  $V_s = -70$  mV,  $I_t = 6.1$  nA].

To confirm the calculation of  $\Delta G(z)$ , we directly probed the probability of finding a single molecule within a certain distance from the substrate. Specifically, for a threshold of  $z_0 = 5.635$  Å, we find a ratio,  $P(z > z_0)/P(z < z_0) \approx 10.99$ , in relatively good agreement with the value 11.76 computed by integration of  $\Delta G(z)$  (see fig. S9 and Materials and Methods). As  $\Delta H_{\text{ads}}$  is increased from  $10k_B T$  to  $16k_B T$  and  $22k_B T$ ,  $\Delta G_{\text{ads}}$  increases accordingly and the probability of finding a single PTCDA molecule near the surface is greatly enhanced (Fig. 4B). Although this follows immediately from the Boltzmann distribution, the situation is more subtle if molecules interact laterally and form a regular surface packing upon adsorption. Thus, we examine self-assembly of PTCDA molecules on a homogeneous Ag(111) substrate as a function of  $\Delta H_{\text{ads}}$ . For molecular adsorption enthalpies of  $10k_B T$  and  $16k_B T$ , we find only moderate adsorption levels (Fig. 4C), as expected from the significant entropy loss upon adsorption. As  $\Delta H_{\text{ads}}$  is increased to  $18k_B T$ , we observe significant surface coverage, with the adsorbed molecules arranged in the herringbone structure found experimentally in Fig. 3 (D and E) (inset of Fig. 4C). An increase of  $\Delta H_{\text{ads}}$  to  $22k_B T$  and  $38k_B T$  does not lead to an appreciable change, but at even higher adsorption enthalpy ( $60k_B T$ ), a large number of defects are observed. We note that these adsorption enthalpies, which lead to almost full surface coverage, are within the range found in density functional theory calculations (0.5 to 3 eV) (37), and we proceed to use  $\Delta H_{\text{ads,Ag}} = 38k_B T$  for the study of competing adsorption on borophene/Ag(111) surfaces. The abrupt in-

crease in surface coverage as a function of  $\Delta H_{\text{ads}}$  is consistent with a first-order transition (Fig. 4C).

To model the formation of lateral heterostructures on heterogeneous substrates of borophene grown on Ag(111), we added a second hexagonally close-packed lattice layer partially covering the original substrate, to represent a borophene island (yellow islands in Fig. 4D). Within the context of our coarse-grained model and considering that the atomic structure of homogeneous-phase borophene is not well established, we chose the same structure for the borophene island to focus on the energy barriers posed by domain edges and, most importantly, the role of competitive binding. The latter is investigated by fixing  $\Delta H_{\text{ads,Ag}}$  on Ag(111) at  $38k_B T$  per molecule and then systematically varying the adsorption enthalpy on borophene,  $\Delta H_{\text{ads,B}}$ . As illustrated in Fig. 4D, PTCDA molecules self-assemble on Ag(111) in all cases and gradually adsorb and self-assemble on the borophene island as  $\Delta H_{\text{ads,B}}$  is increased. As expected, negligible adsorption takes place for  $\Delta H_{\text{ads,B}}$  below  $18k_B T$ . However, even for  $\Delta H_{\text{ads,B}} = 18k_B T$ , where we find full coverage and self-assembly for a homogeneous substrate, low, unordered coverage occurs on the borophene, owing to the competing adsorption by the Ag(111) substrate. Moreover, the energy barrier at the boundary causes the coverage on Ag(111) to terminate abruptly at the edge of the borophene island. Only when  $\Delta H_{\text{ads,B}}$  is increased to  $22k_B T$  could self-assembly occur on both substrates. It is important to note that for the study of competitive binding, the total number of PTCDA molecules in the system must be limited to the

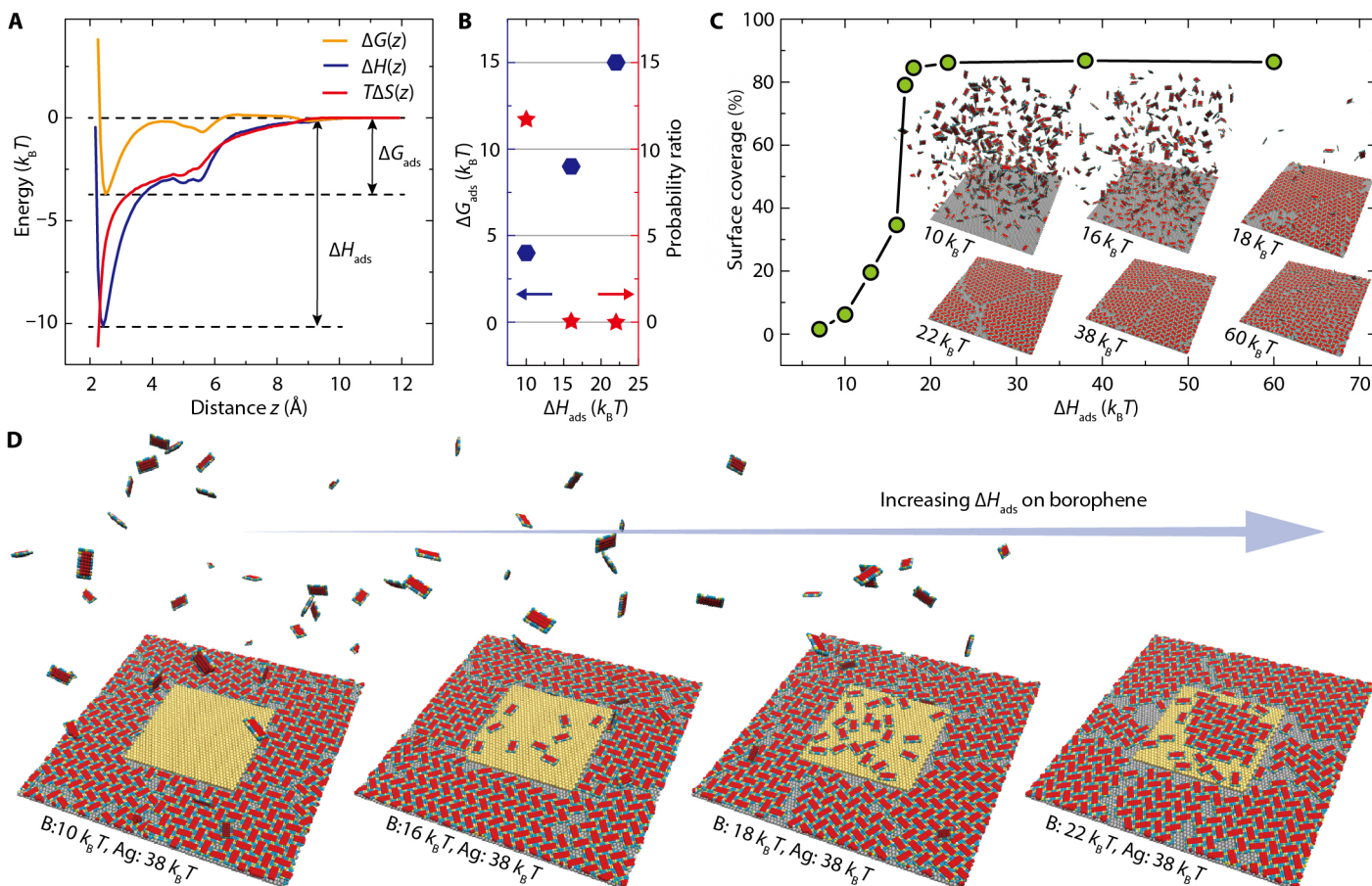


**Fig. 4. MD simulation results.** (A)  $\Delta G(z)$ ,  $\Delta H(z)$ , and  $T\Delta S(z)$  as a function of center-of-mass distance  $z$  to the homogeneous substrate of a single PTCD molecule with  $\Delta H_{\text{ads}} = 10 k_B T$ . (B)  $\Delta G_{\text{ads}}$  and the probability ratio of finding a molecule beyond and within a threshold  $z_0 = 5.635 \text{ \AA}$  from the substrate, as a function of  $\Delta H_{\text{ads}}$ . (C) Surface coverage as a function of  $\Delta H_{\text{ads}}$ . Inset: Simulation snapshots of PTCD adsorption and self-assembly on homogeneous Ag(111) substrates at different  $\Delta H_{\text{ads}}$ . (D) Self-assembled structure of PTCD on heterogeneous borophene/Ag(111) substrates with  $\Delta H_{\text{ads,B}} = 10 k_B T, 16 k_B T, 18 k_B T, \text{ and } 22 k_B T$ .

amount needed for full coverage of the Ag(111). Because our model does not permit multilayer adsorption, at higher PTCD availability, adsorption on borophene will occur as well once the Ag(111) is fully covered and  $\Delta H_{\text{ads,B}}$  is increased to a sufficiently high level. The hydrogen bonding responsible for the formation of the herringbone structure plays a role in suppressing the accumulation of PTCD on the less adsorbing substrate, because molecules cannot form lateral hydrogen bonds at dilute coverage (Fig. 4D, second and third panels). Therefore, within the limitations of the coarse-grained model and the assumption that differences in adsorption are not governed by surface geometry, we find that a PTCD adsorption enthalpy on borophene of less than  $\sim 16 k_B T$  (0.4 eV), combined with a differential in PTCD adsorption enthalpy between Ag(111) and borophene of several  $k_B T$  ( $\sim 0.1$  eV, fig. S10), is sufficient to fully explain the experimental observations. Movies S2 and S3 illustrate the simulated self-assembly process on borophene/Ag(111) surfaces.

#### Spectroscopy of borophene/PTCD lateral heterostructures

Figure 5A displays in situ XPS spectra of borophene before and after PTCD deposition. Consistent with the absence of PTCD on the borophene surface, the B 1s core-level peak is essentially unchanged

following PTCD deposition with the exception of a small downshift ( $< 0.2$  eV) to lower binding energy. On the other hand, in response to the PTCD monolayer on the surrounding Ag(111) surface, the C 1s spectrum in Fig. 5B shows a significant increase in peak intensity, where the two subpeaks at 284.3 and 287.6 eV correspond to the perylene core and carbonyl groups in PTCD (38). The small presence of C preceding PTCD deposition can be attributed to trace amounts of adventitious carbon for Ag on mica (fig. S11). In Fig. 3A, relatively few individual PTCD molecules are present atop borophene, primarily at points that align with underlying Ag step edges. Charge transfer between metallic borophene and these sparsely adsorbed PTCD molecules, as well as the PTCD molecules at the borophene/PTCD lateral heterojunction interface, presumably generates the minor peak shift in the B 1s core-level spectrum. Consistent with this interpretation, charge transfer between PTCD and conventional metallic substrates, including Ag, results in the lowest unoccupied molecular orbital (LUMO) shifting below the Fermi level (19, 25, 37, 39, 40).

To further probe electronic interactions between borophene and PTCD, STS characterization was performed on the borophene/PTCD lateral heterostructure substrate. Specifically, STS spectra are presented in Fig. 5C for clean Ag(111), borophene, and the

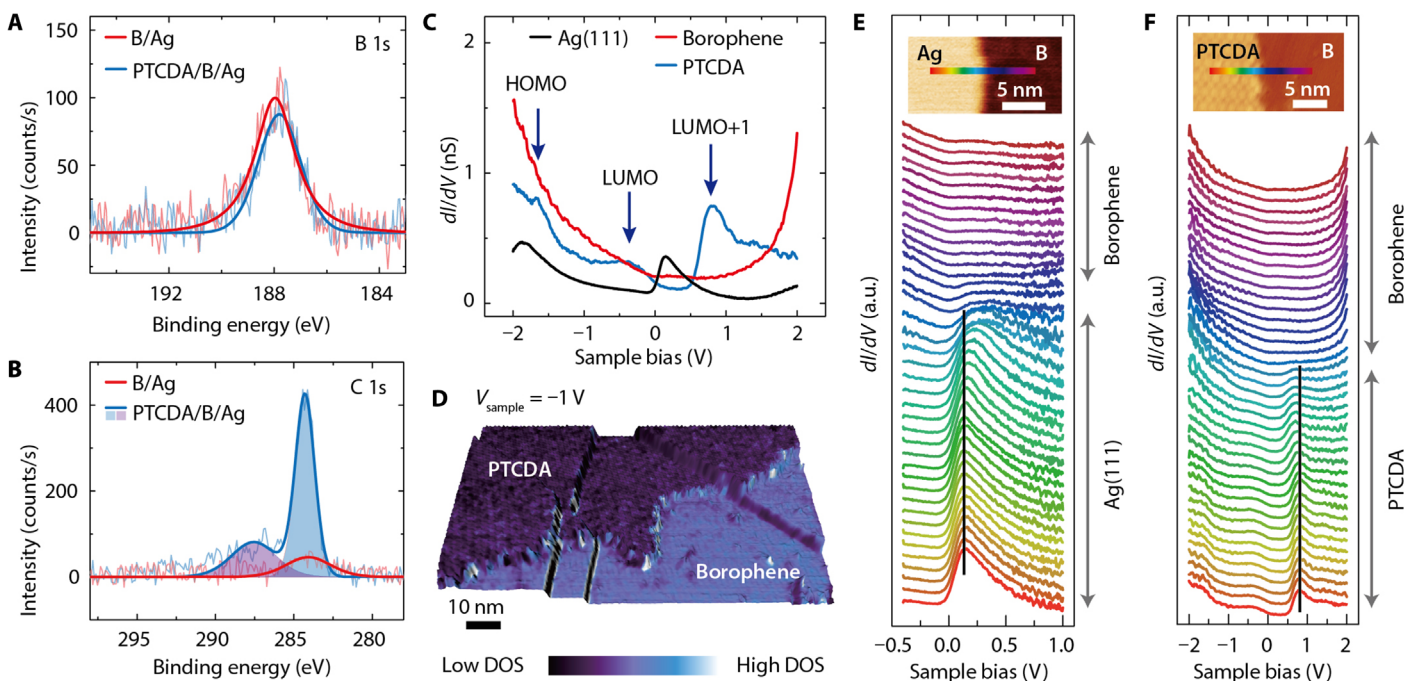


**Fig. 5. Spectroscopic properties of the borophene/PTCDA lateral heterostructure.** (A) In situ XPS spectra of the B 1s core level and (B) C 1s core level before and after the formation of the borophene/PTCDA lateral heterostructure. (C) Differential tunneling conductance spectra of Ag(111), borophene, and PTCDA. HOMO, highest occupied molecular orbital. (D) STS map of a borophene/PTCDA lateral heterostructure overlaid on a three-dimensionally rendered STM topography image ( $V_s = -1$  V,  $I_t = 90$  pA). Spatially resolved STS spectra across the interfaces of (E) borophene/Ag and (F) borophene/PTCDA. The vertical black lines in (E) and (F) indicate the positions of the Ag surface state feature and the LUMO+1 orbital of PTCDA far from the borophene/Ag and borophene/PTCDA interfaces, respectively. a.u., arbitrary units.

PTCDA monolayer. The line shape and features for the PTCDA STS spectrum agree well with literature precedent for the highest occupied molecular orbital ( $-1.7$  eV), LUMO ( $-0.3$  eV), and LUMO+1 ( $0.8$  eV) (25, 37, 40). Figure 5D shows a rendered 3D topography image of the lateral heterostructure with superimposed STS mapping at a sample bias of  $-1$  V. The relative electronic DOS between borophene and PTCDA is in agreement with Fig. 5C. The degree of interfacial electronic interaction is further explored by a series of STS spectra taken across both the Ag/borophene and the PTCDA/borophene interfaces with lateral displacements of  $3.0$  and  $3.8$  Å between adjacent points in Fig. 5 (E and F, respectively). In Fig. 5E, far from the interface, both borophene and Ag(111) show characteristic bulk properties. A small upshift ( $\sim 0.05$  eV) of the Ag surface state feature to higher energy is observed when approaching the interface from Ag(111). The transition in the STS spectra from PTCDA to borophene is abrupt and takes place within  $1$  to  $2$  nm in Fig. 5F, similar to the size of a PTCDA molecule. A small downshift of  $\sim 0.15$  eV of the LUMO+1 state is observed when approaching the junction from PTCDA, likely because of the weak van der Waals interactions between the junction PTCDA molecules and borophene. Compared to the additional features in the STS spectra and the large transition distance due to the presence of edge states and transition regions at MoS<sub>2</sub> edges and grain boundaries (41–43), the borophene/PTCDA lateral heterojunction is noteworthy in terms of its electronic abruptness at the single-nanometer length scale.

## DISCUSSION

In summary, self-assembled borophene/PTCDA lateral heterostructures with structurally and electronically abrupt interfaces have been

realized by sequential deposition of B and PTCDA on Ag(111). The borophene/PTCDA lateral heterostructures occur spontaneously, a finding that is consistent with MD simulations that show that a higher enthalpy of adsorption on Ag(111) and the lateral hydrogen bonding between adsorbed PTCDA molecules lead to the preferential assembly of PTCDA on Ag(111) compared to borophene. The weak chemical interaction between borophene and PTCDA is further corroborated by in situ XPS measurements. Molecular-resolution STM/STS shows that borophene/PTCDA lateral heterostructures are electronically abrupt, with a transition in the DOS from borophene to PTCDA occurring over the length scale of a single PTCDA molecule.

The borophene/PTCDA lateral heterostructure forms a metal/semiconductor lateral heterojunction that has the potential to be exploited in an analogous manner to metal/semiconductor junctions and graphene/organic junctions (44) for electronic applications [for example, resistive switching based on metal/PTCDA/metal junctions (45)]. For these purposes, transfer schemes will need to be developed to realize borophene-based heterostructures on insulating substrates. However, the development of a transfer scheme that does not chemically damage the borophene itself is nontrivial because of the largely unknown chemistry of borophene. The laterally interfacing PTCDA layers could also serve as a template for additional chemistry, thereby facilitating the formation of other borophene heterostructures. Given the lack of knowledge on borophene chemistry, the increasing interest in lateral heterostructures, and the difficulties in obtaining abrupt lateral interfaces free from contamination (12, 17) and alloy formation (13) in other 2D materials, this work represents an important step forward for emerging efforts in borophene-based heterostructures.

**MATERIALS AND METHODS****Growth of borophene/PTCDA lateral heterostructures**

All growth was performed in a UHV preparation chamber (pressure  $< 10^{-9}$  torr) that was directly connected to a loadlock, STM, and XPS system. Ag(111) thin films (~300 nm thick) on mica substrates (Princeton Scientific Corp.) were cleaned by repeated Ar ion sputtering at  $3.3 \times 10^{-6}$  torr (30 min), followed by annealing at 550°C (30 min). The deposition of boron was achieved by electron beam evaporation (SPECS EBE-1) of a pure boron rod (ESPI Metals, 99.9999% purity) onto the cleaned Ag(111) substrates held at 480°C. The deposition flux was measured by the flux electrodes of the evaporator and was maintained at 20 to 28 nA with a filament current of ~5.8 A and an accelerating voltage of 1.3 to 1.6 kV. The typical deposition time is 20 to 30 min to achieve submonolayer coverage of borophene. The electron beam evaporator was housed in a separately pumped chamber with a base pressure of  $8 \times 10^{-11}$  torr, and the boron rod was degassed for >6 hours preceding evaporation. The deposition of PTCDA was achieved by thermally evaporating pure PTCDA molecules (Sigma-Aldrich, 97% purity) in an alumina-coated crucible (R.D. Mathis) in the loadlock chamber ( $2 \times 10^{-9}$  torr) with a heating current of 4.8 A. The molecules were degassed overnight at 2.5 A preceding evaporation. After ramping the current to 4.8 A over 6 min, an exposure time of 1 min resulted in monolayer coverage on Ag(111) substrates, which were maintained at room temperature during deposition.

**STM and spectroscopy**

A home-built UHV STM (46) ( $\sim 10^{-10}$  torr) was used for STM/STS characterization at room temperature with a Lyding design microscope (47). The bias voltage was applied to the sample with respect to the electrochemically etched PtIr tip (Keysight). The piezo scanner was calibrated against the Ag(111) lattice ( $x$ - $y$ ) and atomic step height ( $z$ ). Nanonis (SPECS) control electronics were used for data collection. STS measurements were carried out with a lock-in amplifier (SRS model SR850) with an amplitude of 30 mV<sub>RMS</sub> (millivolts root mean square) and a modulation frequency of ~8.5 kHz. Stable and reproducible spectroscopy was achieved following tip conditioning that included controlled touching of the STM tip to the Ag(111) surface. This process likely leads to the transfer of Ag atoms to the tip apex, which allows for reproducible room temperature spectra on Ag(111), borophene, and PTCDA that are consistent with literature reports (3, 4, 25, 32–34, 37, 40).

**X-ray photoelectron spectroscopy**

In situ XPS spectra were taken with an Omicron DAR 400 M x-ray source (Al K $\alpha$ ), an XM 500 x-ray monochromator, and an EA 125 energy analyzer in a UHV chamber ( $3 \times 10^{-10}$  torr) that was integrated with the STM system and preparation chamber. The XPS energy resolution was 0.6 eV using a pass energy of 20 eV for core-level spectra. Modified Shirley backgrounds were subtracted using Advantage (Thermo Scientific) software. Given the trace amount of adventitious carbon for the clean Ag(111) surface (fig. S11), all peaks were fitted after calibrating the spectra to the Ag 3d<sub>5/2</sub> core-level peak (368.2 eV). This calibration was validated by <0.04 eV changes of the raw Ag 3d<sub>5/2</sub> peaks (fig. S2) for clean Ag(111), borophene/Ag(111), and PTCDA/borophene/Ag(111) in consecutive runs.

**Atomic force microscopy**

Ambient AFM characterization was carried out on an Asylum Cypher AFM in tapping mode. Si cantilevers from NanoWorld

(NCHR-W) were used with a resonant frequency of ~300 kHz. The scanning rate was ~1.5 Hz.

**MD simulations**

The Ag(111) substrate was represented by a hexagonally close-packed lattice of spherical beads with a diameter and interatomic spacing of  $\sigma_{\text{Ag}} = 2.898$  Å. We modeled the coarse-grained PTCDA molecule through a rigid, rectangular collection of  $9 \times 5$  spherical beads (fig. S7), designed on the basis of the hydrogen bonding network (48) and the unit cell of the self-assembled herringbone structure (Fig. 3). The diameter of all PTCDA beads was chosen as  $\sigma = 1.61$  Å (with  $\sigma$  being the LJ unit of length), so that the lateral dimensions of the modeled unit cell closely corresponded to the experimental dimensions (37). Only the beads capable of forming hydrogen bonds in self-assembled PTCDA molecules (fig. S7) had an attractive interaction with the Ag atoms. This attraction is represented by an LJ potential, with an effective length of  $\sigma_{ij} = (\sigma_i + \sigma_j)/2$ , where  $\sigma_{ij} = \sigma_{\text{Ag}}$  or  $\sigma$  and a cutoff of 5.635 Å (shifted to eliminate the LJ potential discontinuity). The adsorption enthalpy of PTCDA was varied by tuning the strength of the LJ potential. All other units in a PTCDA molecule interacted with the substrate via a purely repulsive LJ potential with the same effective length and a cutoff of 2.53 Å (again shifted to eliminate a discontinuity in the potential). Further details of the molecule modeling are given in fig. S7. To study the self-assembly of PTCDA on heterogeneous borophene/Ag(111) substrates, 350 molecules were placed in a simulation box with dimensions of 231.84 Å  $\times$  231.84 Å  $\times$  231.84 Å and periodic boundary conditions in the  $x$  and  $y$  directions. At the upper and lower  $z$  boundaries, purely repulsive LJ walls were placed. The center of the Ag(111) substrate was placed 1.61 Å above the lower  $z$  boundary, and the center of the borophene layer was placed 4.508 Å above the lower  $z$  boundary. To study the self-assembly of PTCDA on homogeneous Ag(111) substrates, 400 molecules were placed in a simulation cell of the same size.

The LAMMPS package was used to perform the MD simulations. The equations of motion were integrated using the velocity-Verlet algorithm. A Langevin thermostat was applied with a temperature of  $1.0\epsilon/k_B$  and a damping time of  $5\tau$ , where  $\epsilon$  and  $\tau$  are the LJ units of energy and time, respectively. The time step was set to  $0.01\tau$ . Each simulation ran for a period of  $1 \times 10^6\tau$  to  $4 \times 10^6\tau$  to reach equilibrium.

To calculate the relative Gibbs free energy  $\Delta G(z)$ , the center of a single PTCDA molecule was placed at a distance  $z$  from the substrate (and centered above a Ag atom), where  $z$  was varied from 11.914 to 2.254 Å with a step size of 0.0805 Å. At each  $z$ , a canonical MD simulation was performed with the center of mass of the molecule fixed to obtain the average force along the  $z$  direction (average forces along the  $x$  and  $y$  directions were confirmed to average out to zero) on the PTCDA molecule. Integration of this ensemble-averaged force with respect to distance from 11.914 to 2.254 Å yielded the Gibbs free energy as a function of  $z$  with respect to the Gibbs free energy of a molecule far from the surface (that is, in free vacuum).

**SUPPLEMENTARY MATERIALS**

Supplementary material for this article is available at <http://advances.sciencemag.org/cgi/content/full/3/2/e1602356/DC1>

fig. S1. Carpet-mode growth of homogeneous-phase borophene.

fig. S2. XPS spectra of Ag 3d and O 1s core levels.

fig. S3. Bias-dependent atomic-resolution images of homogeneous-phase borophene.

fig. S4. Additional atomic-resolution image of borophene.

fig. S5. Growth of PTCDA across various interfaces.

fig. S6. Additional images of PTCDA/borophene lateral heterostructures.

fig. S7. Design of a coarse-grained model for PTCDA.  
 fig. S8. Entropy variation  $\Delta S(z)$  of a single PTCDA molecule as a function of logarithmic distance  $\ln(z - z_{\min})$  to a homogeneous substrate.  
 fig. S9. Probability ratio from thermodynamic integration and single-molecule simulation as a function of threshold  $z_0$  at  $\Delta H_{\text{ads}} = 10k_B T$ .  
 fig. S10. Additional simulated adsorption of PTCDA on borophene/Ag(111).  
 fig. S11. C 1s core-level XPS spectrum of a clean Ag(111) surface.  
 fig. S12. Self-assembled PTCDA on Ag(111).  
 movie S1. STS maps of homogeneous-phase borophene on Ag(111).  
 movie S2. Self-assembly process of PTCDA on heterogeneous borophene/Ag(111) with  $\Delta H_{\text{ads,Ag}} = 38k_B T$  and  $\Delta H_{\text{ads,B}} = 10k_B T$ .  
 movie S3. Self-assembly process of PTCDA on heterogeneous borophene/Ag(111) with  $\Delta H_{\text{ads,Ag}} = 38k_B T$  and  $\Delta H_{\text{ads,B}} = 22k_B T$ .  
 References (49–51)

## REFERENCES AND NOTES

- L. Li, Y. Yu, G. J. Ye, Q. Ge, X. Ou, H. Wu, D. Feng, X. H. Chen, Y. Zhang, Black phosphorus field-effect transistors. *Nat. Nanotechnol.* **9**, 372–377 (2014).
- F.-f. Zhu, W.-j. Chen, Y. Xu, C.-l. Gao, D.-d. Guan, C.-h. Liu, D. Qian, S.-C. Zhang, J.-f. Jia, Epitaxial growth of two-dimensional stanene. *Nat. Mater.* **14**, 1020–1025 (2015).
- A. J. Mannix, X.-F. Zhou, B. Kiraly, J. D. Wood, D. Alducin, B. D. Myers, X. Liu, B. L. Fisher, U. Santiago, J. R. Guest, M. J. Yacaman, A. Ponce, A. R. Oganov, M. C. Hersam, N. P. Guisinger, Synthesis of borophenes: Anisotropic, two-dimensional boron polymorphs. *Science* **350**, 1513–1516 (2015).
- B. Feng, J. Zhang, Q. Zhong, W. Li, S. Li, H. Li, P. Cheng, S. Meng, L. Chen, K. Wu, Experimental realization of two-dimensional boron sheets. *Nat. Chem.* **8**, 563–568 (2016).
- A. R. Oganov, J. Chen, C. Gatti, Y. Ma, Y. Ma, C. W. Glass, Z. Liu, T. Yu, O. O. Kurakevych, V. L. Solozhenko, Ionic high-pressure form of elemental boron. *Nature* **457**, 863–867 (2009).
- A. P. Sergeeva, I. A. Popov, Z. A. Piazza, W.-L. Li, C. Romanescu, L.-S. Wang, A. I. Boldyrev, Understanding boron through size-selected clusters: Structure, chemical bonding, and fluxionality. *Acc. Chem. Res.* **47**, 1349–1358 (2014).
- H. Tang, S. Ismail-Beigi, Novel precursors for boron nanotubes: The competition of two-center and three-center bonding in boron sheets. *Phys. Rev. Lett.* **99**, 115501 (2007).
- X. Wu, J. Dai, Y. Zhao, Z. Zhuo, J. Yang, X. C. Zeng, Two-dimensional boron monolayer sheets. *ACS Nano* **6**, 7443–7453 (2012).
- Y. Liu, E. S. Penev, B. I. Yakobson, Probing the synthesis of two-dimensional boron by first-principles computations. *Angew. Chem. Int. Ed. Engl.* **52**, 3156–3159 (2013).
- E. S. Penev, S. Bhowmick, A. Sadrzadeh, B. I. Yakobson, Polymorphism of two-dimensional boron. *Nano Lett.* **12**, 2441–2445 (2012).
- M. P. Levendorf, C.-J. Kim, L. Brown, P. Y. Huang, R. W. Havener, D. A. Muller, J. Park, Graphene and boron nitride lateral heterostructures for atomically thin circuitry. *Nature* **488**, 627–632 (2012).
- X. Duan, C. Wang, J. C. Shaw, R. Cheng, Y. Chen, H. Li, X. Wu, Y. Tang, Q. Zhang, A. Pan, J. Jiang, R. Yu, Y. Huang, X. Duan, Lateral epitaxial growth of two-dimensional layered semiconductor heterojunctions. *Nat. Nanotechnol.* **9**, 1024–1030 (2014).
- C. Huang, S. Wu, A. M. Sanchez, J. J. P. Peters, R. Beanland, J. S. Ross, P. Rivera, W. Yao, D. H. Cobden, X. Xu, Lateral heterojunctions within monolayer  $\text{MoSe}_2$ - $\text{WSe}_2$  semiconductors. *Nat. Mater.* **13**, 1096–1101 (2014).
- M.-Y. Li, Y. Shi, C.-C. Cheng, L.-S. Lu, Y.-C. Lin, H.-L. Tang, M.-L. Tsai, C.-W. Chu, K.-H. Wei, J.-H. He, W.-H. Chang, K. Suenaga, L.-J. Li, Epitaxial growth of a monolayer  $\text{WSe}_2$ - $\text{MoS}_2$  lateral p-n junction with an atomically sharp interface. *Science* **349**, 524–528 (2015).
- B. Kiraly, A. J. Mannix, M. C. Hersam, N. P. Guisinger, Graphene–silicon heterostructures at the two-dimensional limit. *Chem. Mater.* **27**, 6085–6090 (2015).
- J. Park, J. Lee, L. Liu, K. W. Clark, C. Durand, C. Park, B. G. Sumpter, A. P. Baddorf, A. Mohsin, M. Yoon, G. Gu, A.-P. Li, Spatially resolved one-dimensional boundary states in graphene–hexagonal boron nitride planar heterostructures. *Nat. Commun.* **5**, 5403 (2014).
- B. M. Dhar, G. S. Kini, G. Xia, B. J. Jung, N. Markovic, H. E. Katz, Field-effect-tuned lateral organic diodes. *Proc. Natl. Acad. Sci. U.S.A.* **107**, 3972–3976 (2010).
- P. Sutter, R. Cortes, J. Lahiri, E. Sutter, Interface formation in monolayer graphene–boron nitride heterostructures. *Nano Lett.* **12**, 4869–4874 (2012).
- M. Eremitchenko, J. A. Schaefer, F. S. Tautz, Understanding and tuning the epitaxy of large aromatic adsorbates by molecular design. *Nature* **425**, 602–605 (2003).
- Q. H. Wang, M. C. Hersam, Room-temperature molecular-resolution characterization of self-assembled organic monolayers on epitaxial graphene. *Nat. Chem.* **1**, 206–211 (2009).
- A. A. Zebari, M. Kolmer, J. S. Prauzner-Bechcicki, Characterization of PTCDA nanocrystals on  $\text{Ge}(001):\text{H}(2 \times 1)$  surfaces. *Appl. Surf. Sci.* **332**, 403–408 (2015).
- A. Tekiel, S. Godlewski, J. Budzioch, M. Szymoński, Nanofabrication of PTCDA molecular chains on rutile  $\text{TiO}_2(011)-(2 \times 1)$  surfaces. *Nanotechnology* **19**, 495304 (2008).
- S. A. Burke, W. Ji, J. M. Mativetsky, J. M. Topple, S. Fostner, H.-J. Gao, H. Guo, P. Grütter, Strain induced dewetting of a molecular system: Bimodal growth of PTCDA on NaCl. *Phys. Rev. Lett.* **100**, 186104 (2008).
- S. Kobayashi, T. Nishikawa, T. Takenobu, S. Mori, T. Shimoda, T. Mitani, H. Shimotani, N. Yoshimoto, S. Ogawa, Y. Iwasa, Control of carrier density by self-assembled monolayers in organic field-effect transistors. *Nat. Mater.* **3**, 317–322 (2004).
- R. Temirov, S. Soubatch, A. Luican, F. S. Tautz, Free-electron-like dispersion in an organic monolayer film on a metal substrate. *Nature* **444**, 350–353 (2006).
- A. K. Geim, I. V. Grigorieva, Van der Waals heterostructures. *Nature* **499**, 419–425 (2013).
- Y. Liu, N. O. Weiss, X. Duan, H.-C. Cheng, Y. Huang, X. Duan, Van der Waals heterostructures and devices. *Nat. Rev. Mater.* **1**, 16042 (2016).
- D. Jariwala, T. J. Marks, M. C. Hersam, Mixed-dimensional van der Waals heterostructures. *Nat. Mater.* **10.1038/nmat4703** (2016).
- K. Liu, C. Jin, X. Hong, J. Kim, A. Zettl, E. Wang, F. Wang, Van der Waals-coupled electronic states in incommensurate double-walled carbon nanotubes. *Nat. Phys.* **10**, 737–742 (2014).
- C. W. Ong, H. Huang, B. Zheng, R. W. M. Kwok, Y. Y. Hui, W. M. Lau, X-ray photoemission spectroscopy of nonmetallic materials: Electronic structures of boron and  $\text{B}_x\text{O}_y$ . *J. Appl. Phys.* **95**, 3527–3534 (2004).
- T. T. Xu, J.-G. Zheng, N. Wu, A. W. Nicholls, J. R. Roth, D. A. Dikin, R. S. Ruoff, Crystalline boron nanoribbons: Synthesis and characterization. *Nano Lett.* **4**, 963–968 (2004).
- J. Li, W.-D. Schneider, R. Berndt, Local density of states from spectroscopic scanning-tunneling-microscope images: Ag(111). *Phys. Rev. B* **56**, 7656–7659 (1997).
- J. Li, W.-D. Schneider, R. Berndt, O. R. Bryant, S. Crampin, Surface-state lifetime measured by scanning tunneling spectroscopy. *Phys. Rev. Lett.* **81**, 4464–4467 (1998).
- J. Li, W.-D. Schneider, R. Berndt, B. Delley, Kondo scattering observed at a single magnetic impurity. *Phys. Rev. Lett.* **80**, 2893–2896 (1998).
- S. Orisaka, T. Minobe, T. Uchihashi, Y. Sugawara, S. Morita, The atomic resolution imaging of metallic Ag(111) surface by noncontact atomic force microscope. *Appl. Surf. Sci.* **140**, 243–246 (1999).
- R. Otero, J. M. Gallego, A. L. Vázquez de Parga, N. Martín, R. Miranda, Molecular self-assembly at solid surfaces. *Adv. Mater.* **23**, 5148–5176 (2011).
- M. Rohlfing, R. Temirov, F. S. Tautz, Adsorption structure and scanning tunneling data of a prototype organic-inorganic interface: PTCDA on Ag(111). *Phys. Rev. B* **76**, 115421 (2007).
- J. Wüsten, T. Ertl, S. Lach, C. Ziegler, Post deposition purification of PTCDA thin films. *Appl. Surf. Sci.* **252**, 104–107 (2005).
- F. S. Tautz, M. Eremitchenko, J. A. Schaefer, M. Sokolowski, V. Shklover, E. Umbach, Strong electron-phonon coupling at a metal/organic interface: PTCDA/Ag(111). *Phys. Rev. B* **65**, 125405 (2002).
- A. Kraft, R. Temirov, S. K. M. Henze, S. Soubatch, M. Rohlfing, F. S. Tautz, Lateral adsorption geometry and site-specific electronic structure of a large organic chemisorbate on a metal surface. *Phys. Rev. B* **74**, 041402 (2006).
- X. Liu, I. Balla, H. Bergeron, G. P. Campbell, M. J. Bedzyk, M. C. Hersam, Rotationally commensurate growth of  $\text{MoS}_2$  on epitaxial graphene. *ACS Nano* **10**, 1067–1075 (2016).
- X. Liu, I. Balla, H. Bergeron, M. C. Hersam, Point defects and grain boundaries in rotationally commensurate  $\text{MoS}_2$  on epitaxial graphene. *J. Phys. Chem. C* **120**, 20798–20805 (2016).
- Y. L. Huang, Y. Chen, W. Zhang, S. Y. Quek, C.-H. Chen, L.-J. Li, W.-T. Hsu, W.-H. Chang, Y. J. Zheng, W. Chen, A. T. S. Wee, Bandgap tunability at single-layer molybdenum disulfide grain boundaries. *Nat. Commun.* **6**, 6298 (2015).
- K. Kim, T. H. Lee, E. J. G. Santos, P. S. Jo, A. Salleo, Y. Nishi, Z. Bao, Structural and electrical investigation of  $\text{C}_{60}$ -graphene vertical heterostructures. *ACS Nano* **9**, 5922–5928 (2015).
- R. Agrawal, P. Kumar, S. Ghosh, Mechanism of resistive switching in 3, 4, 9, 10 perylene-tetracarboxylic dianhydride (PTCDA) sandwiched between metal electrodes. *IEEE Trans. Electron Devices* **55**, 2795–2799 (2008).
- E. T. Foley, N. L. Yoder, N. P. Guisinger, M. C. Hersam, Cryogenic variable temperature ultrahigh vacuum scanning tunneling microscope for single molecule studies on silicon surfaces. *Rev. Sci. Instrum.* **75**, 5280–5287 (2004).
- R. T. Brockenbrough, J. W. Lyding, Inertial tip translator for a scanning tunneling microscope. *Rev. Sci. Instrum.* **64**, 2225–2228 (1993).
- C. Weiss, C. Wagner, R. Temirov, F. S. Tautz, Direct imaging of intermolecular bonds in scanning tunneling microscopy. *J. Am. Chem. Soc.* **132**, 11864–11865 (2010).

49. R. A. Pollak, L. Ley, F. R. McFeely, S. P. Kowalczyk, D. A. Shirley, Characteristic energy-loss structure of solids from X-ray photoemission spectra. *J. Electron. Spectrosc. Relat. Phenom.* **3**, 381–398 (1974).
50. E. Espinosa, E. Molins, C. Lecomte, Hydrogen bond strengths revealed by topological analyses of experimentally observed electron densities. *Chem. Phys. Lett.* **285**, 170–173 (1998).
51. Y. Azuma, K. Iwasawa, T. Kurihara, K. K. Okudaira, Y. Harada, N. Ueno, Low energy electron diffraction of the system In-[perylene-3,4,9,10-tetracarboxylic dianhydride] on MoS<sub>2</sub>. *J. Appl. Phys.* **91**, 5024–5028 (2002).

**Acknowledgments:** We thank J. D. Wood and M. Han for valuable discussions. **Funding:** This work was supported by the Office of Naval Research (ONR N00014-14-1-0669) and the Northwestern University Materials Research Science and Engineering Center (NSF DMR-1121262). MD simulations were conducted on computing facilities provided through the User Nanoscience Research Program at the Center for Nanophase Materials Sciences, which is a U.S. Department of Energy Office of Science User Facility. **Author contributions:** X.L. and M.C.H. conceived the experiments. X.L. performed sample preparation, STM/STS,

and AFM characterization. Z.W. and E.L. designed the model, and Z.W. performed MD simulations. X.L. and I.B. performed XPS experiments and data processing. A.J.M. provided assistance with borophene growth. All authors contributed to data interpretation and manuscript writing. **Competing interests:** The authors declare that they have no competing interests. **Data and materials availability:** All data needed to evaluate the conclusions in the paper are present in the paper and/or the Supplementary Materials. Additional data related to this paper may be requested from the authors

Submitted 25 September 2016

Accepted 9 January 2017

Published 22 February 2017

10.1126/sciadv.1602356

**Citation:** X. Liu, Z. Wei, I. Balla, A. J. Mannix, N. P. Guisinger, E. Luijten, M. C. Hersam, Self-assembly of electronically abrupt borophene/organic lateral heterostructures. *Sci. Adv.* **3**, e1602356 (2017).

This article is published under a Creative Commons license. The specific license under which this article is published is noted on the first page.

For articles published under **CC BY** licenses, you may freely distribute, adapt, or reuse the article, including for commercial purposes, provided you give proper attribution.

For articles published under **CC BY-NC** licenses, you may distribute, adapt, or reuse the article for non-commercial purposes. Commercial use requires prior permission from the American Association for the Advancement of Science (AAAS). You may request permission by clicking [here](#).

***The following resources related to this article are available online at <http://advances.sciencemag.org>. (This information is current as of February 22, 2017):***

**Updated information and services**, including high-resolution figures, can be found in the online version of this article at:

<http://advances.sciencemag.org/content/3/2/e1602356.full>

**Supporting Online Material** can be found at:

<http://advances.sciencemag.org/content/suppl/2017/02/17/3.2.e1602356.DC1>

This article **cites 50 articles**, 3 of which you can access for free at:

<http://advances.sciencemag.org/content/3/2/e1602356#BIBL>

*Science Advances* (ISSN 2375-2548) publishes new articles weekly. The journal is published by the American Association for the Advancement of Science (AAAS), 1200 New York Avenue NW, Washington, DC 20005. Copyright is held by the Authors unless stated otherwise. AAAS is the exclusive licensee. The title *Science Advances* is a registered trademark of AAAS